

Calibration and Performance of the AKARI Far-Infrared Surveyor (FIS) — Slow-Scan Observation Mode for Point Sources

Mai SHIRAHATA¹, Shuji MATSUURA¹, Sunao HASEGAWA¹, Takafumi OOTSUBO¹, Sin'itirou MAKIUTI¹, Issei YAMAMURA¹, Takao NAKAGAWA¹, Mitsunobu KAWADA², Hidehiro KANEDA², Hiroshi SHIBAI^{3,2}, Yasuo DOI⁴, Toyoaki SUZUKI⁵, Thomas MÜLLER⁶, and Martin COHEN⁷

¹*Institute of Space and Astronautical Science (ISAS), Japan Aerospace Exploration Agency (JAXA), 3-1-1 Yoshinodai, Sagami-hara, Kanagawa 229-8510
sirahata@ir.isas.jaxa.jp*

²*Graduate School of Science, Nagoya University, Furo-cho, Chikusa-ku, Nagoya 464-8602*

³*Graduate School of Science, Osaka University, 1-1 Machikaneyama-cho, Toyonaka-shi, Osaka 560-0043*

⁴*Department of General System Studies, Graduate School of Arts and Science, The University of Tokyo, 3-8-1 Komaba, Meguro-ku, Tokyo 153-8902*

⁵*National Astronomical Observatory of Japan, National Institutes of Natural Sciences, 2-21-1 Osawa, Mitaka, Tokyo 181-8588*

⁶*Max-Planck-Institut für extraterrestrische Physik, Giessenbachstrasse, 85748 Garching, Germany*

⁷*Radio Astronomy Laboratory, 601 Campbell Hall, University of California, Berkeley, CA 94720, USA*

(Received 2008 October 8; accepted 2009 April 16)

Abstract

We present the characterization and calibration of the Slow-Scan observation mode of the Far-Infrared Surveyor (FIS) onboard the AKARI satellite. The FIS, one of the two focal-plane instruments on AKARI, has four photometric bands between 50–180 μm with two types of Ge:Ga array detectors. In addition to the All-Sky Survey, FIS has also taken detailed far-infrared images of selected targets by using the Slow-Scan mode. The sensitivity of the Slow-Scan mode is one to two orders of magnitude better than that of the All-Sky Survey, because the exposure time on a targeted source is much longer. The point spread functions (PSFs) were obtained by observing several bright point-like objects such as asteroids, stars, and galaxies. The derived full widths at the half maximum (FWHMs) are $\sim 30''$ for the two shorter wavelength bands and $\sim 40''$ for the two longer wavelength bands, being consistent with those

expected by the optical simulation, although a certain amount of excess is seen in the tails of the PSFs. The flux calibration has been performed by the observations of well-established photometric calibration standards (asteroids and stars) in a wide range of fluxes. After establishing the method of aperture photometry, the photometric accuracy for point-sources is better than $\pm 15\%$ in all of the bands expect for the longest wavelength.

Key words: instrumentation: detectors — space vehicles — techniques: photometric — methods: data analysis

1. Introduction

AKARI is the first Japanese satellite dedicated to infrared astronomy (Murakami et al. 2007). It was successfully launched on February 21st in 2006 (UT) from the Uchinoura Space Center (USC) with the M-V rocket of Japan Aerospace Exploration Agency (JAXA). AKARI opened its aperture lid to begin astronomical observation on April 13th 2006. AKARI achieved continuous observation during 550 days by the time when the liquid-helium ran out on August 26th 2007. AKARI was thrown in a sun-synchronous polar orbit along the twilight zone at an altitude of ~ 700 km in order to carry out the All-Sky Survey in every half-year. The telescope has the size of 68.5 cm in diameter (Kaneda et al. 2007), and is cooled down at lower than 6 K in a liquid-helium cryostat (Nakagawa et al. 2007) for reduction of thermal emission from the instruments.

The Far-Infrared Surveyor (FIS) is one of the two focal-plane instruments onboard AKARI (Kawada et al. 2007). It has four photometric bands between 50–180 μm , with two types of Ge:Ga array devices; the Short-Wavelength (SW) detector and the Long-Wavelength (LW) detector. The SW detector (Fujiwara et al. 2003), which is responsible for the wavelength range in 50–110 μm , is a two-dimensional monolithic Ge:Ga photoconductor array. This array is directly connected to a cryogenic readout electronics (CRE) by Indium-bumping technology. This detector was developed under collaboration among the National Institute of Information and Communications Technology (NICT), Institute of Space and Astronautical Science (ISAS) of Japan Aerospace Exploration Agency (JAXA), and Nagoya University. On the other hand, the LW detector (Doi et al. 2002) for 110–180 μm is a compact stressed Ge:Ga photoconductor array having a special cavity structure and a stressing mechanism. Ge:Ga chips for the LW detector were supplied by NICT, and the LW detector module was assembled by the University of Tokyo. As for the CREs of the SW and LW detectors, we developed a Capacitive Trans-Impedance Amplifier (CTIA) with silicon p-MOSFETs optimized for low-temperature operation (Nagata et al. 2004). FIS was designed primarily to perform the All-Sky Survey, which is the main purpose of the AKARI mission. Additionally, FIS has two other operation modes with pointing attitude control; the Slow-Scan mode to take detailed images of specific

targets and the spectroscopy mode to take spectra by using the Fourier transform spectrometer (Kawada et al. 2008; Murakami et al. 2009, in prep.). The sensitivity in the Slow-Scan mode is 1–2 orders of magnitude better than that of the All-Sky Survey, because the exposure time on a target source is longer than the All-Sky Survey mode. In this paper, we describe the data reduction procedures and the in-orbit performance of the Slow-Scan mode, the imaging performance, and the flux calibration.

Characterization and calibration of FIS were performed by observing two kinds of well-established photometric calibration standards. One of them are solar-system objects such as asteroids and planets, and the others are stars. These calibration sources were studied well enough (asteroids; Müller & Lagerros 1998, 2002, stars; Cohen et al. 1999, 2003a, 2003b), and were used as the calibration standard in the previous infrared missions (e.g., ISO/ISOCAM; Blommaert et al. 2003, ISO/ISOPHOT; Schulz et al. 2002, COBE/DIRBE; Hauser et al. 1998, and Spitzer/MIPS; Gordon et al. 2007, Stansberry et al. 2007). Some of the galaxies observed by ISO and IRAS were also examined not only for the cross calibration but also for the calibration check for the objects with much redder spectra than stars and asteroids.

In Sec. 2, we explain the method of the FIS Slow-Scan observation. We describe observations of the calibration standards in Sec. 3. Careful data reduction procedures are required in order to obtain high-quality images and to establish the accurate calibration. Accordingly, we describe the process of data reduction in Sec. 4. The imaging performance is discussed in Sec. 5. In Sec. 6, we describe the calibration factors, and their flux dependency by considering the characteristics of the Ge:Ga detectors. We also checked the consistency of the calibration for various observations. Finally, we summarize our results in Sec. 7. The calibration factors derived by the present work are the official values of AKARI/FIS Slow-Scan calibration.

2. FIS Slow-Scan Observation

The FIS has four photometric bands whose center wavelengths are represented at 65, 90, 140, and 160 μm . These band shapes, shown in Fig. 1, are formed by the combination of optical filters and two detector devices. Each detector device covers one broad-band and one narrow-band; *WIDE-S* (90 μm) and *N60* (65 μm) for the SW detector and *WIDE-L* (140 μm) and *N160* (160 μm) for the LW detector. The array formats are 3×20 , 2×20 , 3×15 , and 2×15 for the *WIDE-S*, *N60*, *WIDE-L*, and *N160* bands, respectively. The pixel scales are 26.8 arcsec for the SW detector and 44.2 arcsec for the LW detector, whose values are comparable to the diffraction limits of the telescope. The field-of-views (FOVs) of two detector devices overlap on the sky. The specifications for the FIS instrument are summarized in Tab. 1.

As reported by many authors, Ge:Ga detectors show slow transient response at low temperature under low background flux conditions, i.e., in the space environment (Kaneda et al. 2002, Hiromoto & Fujiwara 1999, Haegel et al. 1999, Fouks & Schubert 1995, and references therein). This slow transient response indicates time-delay in response for quick changes of

the incoming flux. The time constant of the slow response is typically 10–100 seconds, and it depends on both the background and the signal photon fluxes. Therefore, in the case of AKARI which conduct the scan observations, the slow response causes decrease of the sensitivity for compact sources. In order to reduce the effects of the slow response of the LW detector, an offset light source is placed in front of the LW detector unit to irradiate each detector pixels with a constant intensity. The intensity of this offset light source was set to be ~ 100 MJy sr^{-1} to obtain the highest signal-to-noise ratio taking the increase of the photon noise into account.

The FIS Slow-Scan observations are carried out using the AKARI astronomical observation templates (AOTs) FIS01 and FIS02. FIS01 is designed for compact source photometry with two sets of round-trip scans, while FIS02 is suitable for wide area mapping with a long single round-trip scan. Observers can select the scan speed ($8'' \text{ s}^{-1}$ or $15'' \text{ s}^{-1}$) and the reset interval (0.5 sec, 1.0 sec, or 2.0 sec). In case of FIS01, the cross-scan shift length between two round trips is also selectable from either a few pixels ($70''$) or half of the FOV ($240''$). More details about the AOTs are described in Kawada et al. (2007) and Verdugo et al. (2007).

One set of the Slow-Scan observation takes about 30 minutes, including the calibration sequence. The dark current measurement and responsivity check with an internal calibrator are executed by closing the cold shutter during 7 minutes of the attitude maneuver operation between the All-Sky Survey position and the target position of the pointing observation. After the maneuver completes, the shutter is opened for monitoring the sky signal during the settling time for fine control of the satellite attitude, and then the Slow-Scan starts. At the turning point(s) of the round-trip scan(s), the shutter is briefly closed and the internal calibration lamps are turned on to monitor the time variation of the detector responsivity. The total observation time for the round-trip scan(s) is about 12 minutes. The same calibration sequence is repeated during the maneuver for returning to the All-Sky Survey mode after the pointing observation. Such a highly-redundant calibration data set enabled us to correct the response changes of the detectors, referring to astronomical calibration data taken by separate observations with the same calibration sequence.

3. Targets

For evaluation of the imaging performance and flux calibration, several kinds of astronomical point-like sources were observed; 18 Slow-Scan observations of 14 stars, 17 Slow-Scan observations of 11 asteroids, 2 Slow-Scan observations of a planet (Neptune), and 13 Slow-Scan observations of 11 galaxies. All observations were carried out by the FIS01 (two round-trip scans) mode with a $70''$ shift. The scan speed was $8'' \text{ s}^{-1}$ for most cases to obtain a high signal-to-noise ratio. A few observations were performed with the $15'' \text{ s}^{-1}$ scan in order to check the influence caused by the differences of the scan speed. The reset interval was chosen so as to avoid saturation for each target.

The calibration stars were selected from the standard star catalog for spectral types of

AV and *KIII* established by M. Cohen et al. (1999, 2003a, 2003b). These stars have been studied extensively and are reliable as the calibration standards with the accuracies better than 6%. Unfortunately, the stars are too faint to use as calibrators for the *WIDE-L* and *N160* bands.

Since asteroids are brighter than stars, they are widely used as the far-infrared calibrators (Müller & Lagerros 2003). We used them for the *N60* and *WIDE-S* bands and also for the *WIDE-L* and *N160* bands. Asteroids show flux variations on various levels and time scales due to the change of illumination, observing geometries, and also their rotation. Therefore, we estimated the expected flux for each observation from the thermophysical model (TPM) (Müller & Lagerros 1998, 2002) by taking the geometries and surface properties into account. The flux uncertainties (see Tab. 2) are based on a thorough analysis of the TPM input parameters and the number and quality of well-calibrated thermal observations for each asteroid. The apparent motions of the asteroids are typically less than $1'$ hour⁻¹, and are taken into account at image co-addition (see Fig. 2).

We also observed several point-like galaxies (luminous infrared galaxies) whose fluxes have been well studied by IRAS and ISO. We used bright samples for the measurement of the point spread functions (PSFs) and the encircled energy functions, especially for the *N160* band.

Table 2 summarizes the observation log and the expected fluxes with their uncertainties. In all the four bands, the expected fluxes range from ~ 100 mJy to ~ 100 Jy, i.e., more than three orders of magnitudes. Note that the expected fluxes listed here are color-corrected values by assuming the flat spectrum (i.e., $\nu F_\nu = \text{const.}$). All observations had been carried out in the performance verification (PV) phase and in the engineering time available for calibration which is occasionally allocated according to the requirement.

4. Data Reduction

The raw data were processed using the official FIS slow-scan data-analysis toolkit (SS-tool) to produce the time-series calibrated data and the final co-added map. More details about the standard reduction steps are described in Matsuura et al. (2007).

First of all, the raw data were processed by the software tools to do ADU-to-volt conversion, flagging of bad data (dead pixels, saturated pixels, reset anomalies, and other discontinuities) and the correction of non-linear integration ramps.

The next process is slope calculation of each ramp, removing the cosmic-ray events identified in the ramp. This process maximizes the signal-to-noise ratio and avoids any periodic structure arising from incompleteness of the non-linear ramp correction. The reduced data provides 1–10 samples per pixel for a source crossing time, which depend on both the scan speed and the reset interval. By co-adding the data of all array pixels, the Nyquist sampling condition is satisfied in the real-space domain. Glitches and subsequent tails induced by cosmic-ray hits affect the data severely (Suzuki et al. 2008). The integration ramps affected by the

glitches were eliminated in the slope calculation process. The tails were not flagged-out at this stage, but the affected data were removed by sigma clipping in the co-addition process.

The third step of the SS-tool processing is to produce calibrated data for each array pixel after dark current subtraction and flat-fielding. The pixel-to-pixel variations of the detector responsivity are approximately 15% and 50% of the average for the SW detector and the LW detector, respectively. Therefore, the correction of the responsivity variation is necessary to obtain accurate images. This process is based on the FIS observations of known diffuse sources: zodiacal emissions and interstellar dust emissions, which are expected to be smooth within the field of view. In this process we can also compare the sky brightness measured by the FIS with DIRBE/COBE, which provide a well calibrated far-infrared sky map (Matsuura et al., in prep.). Accordingly, the unit conversion from the instrumental unit to the surface brightness is simultaneously performed.

The zodiacal emission is expected to be almost perfectly flat; their anisotropies on arcminute scales are less than 1% (Abraham et al. 1997). In the cases of the *N60* and *WIDE-S* bands, the sky brightness of almost entire sky except for the Galactic Plane regions is dominated by the zodiacal emission, and the contributions of galactic cirrus (interstellar dust) emission are expected to be negligible. Hence, the blank sky observed near the target source can be used for flat-fielding, as long as there is no bright source in there. The response distribution of the detector array pixels is derived from the average of time-series data during the Slow-Scan, where the average is calculated after removing data that exceed the $3\text{-}\sigma$ noise level for each pixel. The flat is built based on sky monitoring data acquired during the attitude-settling time just before the Slow-Scan observation. The flat-fielding is done by dividing the data by the response distribution. With this 'self' flat-fielding method, any stripes in the image caused by the flat field errors are buried under the random noise.

In the cases of the *WIDE-L* and *N160* bands, the detector signals are dominated by offset light implemented to improve the slow transient response of the stressed Ge:Ga. Although galactic cirrus emissions at high latitudes could be a flat source with moderate smoothness ($\sim 10\%$) and relatively high brightness, their signals are less than 10% of that of the offset light. The intensity distributions of the offset light at the aperture of the detector arrays are estimated from laboratory measurements to be uniform to within 10%. Hence, the 'self' flat-fielding method with an average sky signal including offset light was applied to correct the responsivity variation in the detector arrays, as was done for the *N60* and *WIDE-S* bands.

The final step of the SS-tool processing is co-addition of the calibrated time-series data onto a sky grid. The sky position of each data point is derived from the telescope boresight according to the satellite attitude and from the array pixel map on the focal-plane. The grid pixel sizes were set to $2''5$. A sufficient number of data point per grid pixel (>5 on average) is secured by considering the finite size of the detector array pixel (Drizzle method; Williams et al. 1996). In the co-adding process, small glitches and other artifacts were sigma-clipped with

the standard deviation calculated at each grid pixel. The threshold for the sigma-clipping was set to 5-times the standard deviation. The fraction of the rejected data points in this process was less than 1% of the original data.

Figure 2 shows an example of the final co-added images (asteroid Ceres) for all the FIS bands. The imaging performance and flux calibration based on the obtained maps are discussed in the following section.

5. Imaging Performance

5.1. Point Spread Functions (PSFs)

Before the launch of AKARI, we checked the PSFs in the laboratory using a pin-hole source located on the focal-plane of the FIS optics (Shirahata et al. 2003). The measured PSFs were almost consistent with those expected from the optical simulation, though the uncertainty originated in the measurement system was somewhat large. The PSFs, throughout the optics including the AKARI telescope, were evaluated in orbit by observations of bright point-sources. These sources are chosen with the condition that S/N for single pointing observation is better than 300, which are designated in Tab. 2 by the bold-faced type or the circle symbols; 19 sources brighter than 10 Jy for the *N60* band, 28 sources brighter than 2 Jy for the *WIDE-S* band, 6 sources brighter than 20 Jy for the *WIDE-L* band, and 4 sources brighter than 50 Jy for the *N160* band. Figure 3 shows the azimuthally-averaged radial profiles of the measured PSFs and compares them to the optical simulation model (Jeong et al. 2003). The averaged profiles are well reproduced by the two-component Gaussian functions, whose parameters are summarized in Tab. 3. The full widths at the half maximum (FWHM) of the main Gaussian component are 32 ± 1 , 30 ± 1 , 41 ± 1 , and 38 ± 1 arcsec for the *N60*, *WIDE-S*, *WIDE-L*, and *N160* bands, respectively. At the tails of the PSFs, there are significant excess compared with the optical simulation, whose contributions are about 20% of the total power. We did not see any significant dependence in the PSFs on the infrared color of the targets.

5.2. Cross-talk and Ghost Signals

One property affecting the imaging quality is cross-talk between array pixels. This effect is seen only with the SW detector, which has a monolithic structure. In the maps of the SW detector (*N60* and *WIDE-S*) shown in Fig. 2, cross-talk signals are clearly seen along the detector array axes. Amplitude of the cross-talk signal is roughly 5% or less of the peak signal. Possibility to explain this phenomenon is carrier diffusion or internal-reflection in the Ge:Ga substrate.

Another concern in terms of imaging quality is the presence of ghost signals. A ghost image appears in the all bands near the target image, and is prominent especially for the *N160* band as shown in Fig. 2. The center positions of broad-band and narrow-band arrays have an angular separation of ~ 6 arcmin in the scanning direction, and the ghost signal of each

array appears separate time corresponding to the angular separation. Therefore, the ghost signal appears in one array when a strong light enters the other array of the same detector. The cause of the ghost is presumably electrical cross-talk in the multiplexer of the cryogenic readout electronics. The position and intensity of the ghost signal to the target signal, which are summarized in Tab. 4, had been stable throughout the mission. As long as the target is a point-source, the ghost should be removable.

6. Flux Calibration

6.1. Calibration Factor

As described in Sec. 4, the final co-added maps produced by the SS-tool have units of surface brightness in MJy sr⁻¹, which has been calibrated in the earlier stage in the data processing by diffuse sources such as the zodiacal emission and the interstellar dust emission (Matsuura et al. in prep.). The application of aperture photometry for the co-added map gives the temporal flux of the target source. Hereafter, we derive the calibration factors for point-source photometry based on the observations of the calibration standards.

For the source extraction and the aperture photometry, we used the photometry tools FIND, GCENTRD, and APER in the IDL Astronomy User’s Library (Landsman 1993) at NASA/GSFC. These tools search for the center positions of point-sources with a Gaussian window function of the same width as the PSF, and measure the fluxes by integrating the pixel values within the aperture. The background sky levels were estimated to be the average of the surface brightness in the sky annulus, defined as 2’3–3’3 in radius for the *WIDE-S* and *N60* bands, and 3’0–4’0 for the *WIDE-L* and *N160* bands, respectively. The inner radius of the sky annulus is distant enough from the target source, and the outer radius is distant enough from the edges of the maps.

Before performing the aperture photometry for all of the calibration standards, we compounded the encircled energy functions from the images of the bright sources that were used to measure the PSFs. First we computed the encircled energy for each source with various aperture radii, and then normalized the result at the background sky flux level. The obtained profiles of the encircled energy show good agreement with each other, within ~3% for the shorter 3-bands and ~6% for the *N160* band, as shown in Fig. 4. The aperture correction factors as the normalized encircled energy functions are summarized in Tab. 5.

We performed aperture photometry on all images of the calibration standards by using the aperture radius of 40” for the *WIDE-S* and *N60* bands, and 60” for the *WIDE-L* and *N160* bands, respectively, and applied the aperture correction with the factors tabulated in Tab. 5. These aperture radii are large enough to minimize uncertainties due to centroiding errors and to ensure that any uncertainties in the aperture correction have a small effect on the derived fluxes. In addition, these aperture sizes enable us to improve the S/N of the photometry and

thereby to extend the calibration to the sources with somewhat fainter flux densities. We derive the uncertainty on each measurement from the scatter of the pixel values in the background annulus, which contributes both the uncertainty due to summing the object flux density as well as subtracting the background.

In order to derive the calibration factor for the point-source photometry, we compared the observed fluxes obtained by the aperture photometry with their model prediction. Figure 5 shows the observed-to-expected flux ratios for the calibration standards as a function of the expected flux. Two asteroids (Germania and Iris) are excluded from the plot because of their poor model accuracies. The uncertainty on the flux ratios includes both photometric error and the expected model flux of the calibration standard. As shown in Fig. 5, even after the aperture correction, the observed fluxes are always lower than the expected fluxes. This means that the sensitivity to the point-sources is lower than that to the diffuse sources. In addition, the deviation seems to have flux-dependency. A plausible cause of this disagreement is the slow transient response of the Ge:Ga detectors. Prior to the launch of AKARI, we had measured the slow response systematically under various photon flux conditions and established an empirical model (Kaneda et al. 2002). According to the model, the slow response should depend on the total photo-current (background plus signal).

Figure 6 shows the observed-to-expected flux ratios, as a function of the total observed flux including the background. The observed background used here is the sum of the background sky brightness and the detector dark current. In order to convert the units of the background from MJy sr⁻¹ to Jy, the beam solid angle derived from the PSF, which is summarized in Tab. 6, is multiplied.

As described in Sec. 2, the reset interval was changed depending on the source flux. In Fig. 6, different symbols denote data with different reset intervals. Because no systematic differences were seen, we deal with these data equally.

In the SW bands, the background flux is so small that the total flux is dominated by the source flux. We can see a clear trend, the higher the total flux, the smaller the ratio. For bright sources, the ratio is ~ 0.5 , while for faint sources, the ratio is ~ 0.8 , although they show large scatter. Solid lines in Fig. 6 are the results of power-law fitting to the data. The fitting results give

$$\begin{aligned} \text{Ratio} &= (0.698 \pm 0.015) \times (\text{Total Flux})^{(-0.0659 \pm 0.0089)} && \text{for the } N60 \text{ band,} \\ \text{Ratio} &= (0.700 \pm 0.013) \times (\text{Total Flux})^{(-0.0757 \pm 0.0085)} && \text{for the } WIDE-S \text{ band.} \end{aligned}$$

The deviations of the data from the power-law are reasonably small, 13.7% and 12.7% for the *N60* and *WIDE-S* bands, respectively. If we assume that the ratio is constant, the weighted means are 0.603 ± 0.007 and 0.607 ± 0.008 for the *N60* and *WIDE-S* bands, respectively, and the deviation increases to approximately 20% for both bands. Therefore, we conclude that there is a significant trend in the ratio with the total flux due to the slow transient response of the

Ge:Ga detectors, and adopted the fitting results as the flux-dependent calibration factors.

In contrast to the case of the SW bands, the total fluxes in the LW bands are dominated by the offset light. Therefore, the total flux range is limited small, and the flux ratio does not show a clear flux dependence. Unfortunately for the *N160* band, a few data points does not give a firm conclusion but can suggest a trend as well as the *WIDE-L* band. No dependence of the flux ratio on the small flux range has been expected from an empirical model of stressed Ge:Ga photoconductor (Kaneda et al. 2002). The weighted means of the ratio in Fig. 6 are 0.560 ± 0.011 and 0.277 ± 0.011 for the *WIDE-L* and *N160* bands, respectively. The results show that the LW detectors have much slower response than the SW detectors despite that it uses offset light to improve the slow transient response. The deviations of the data from the weighted means are 9.97% and 50.5% for the *WIDE-L* and *N160* bands, respectively. The calibration accuracy of the *N160* band are much lower than the other bands because of the small number of samples.

6.2. Validity of the Calibration

In this subsection, we perform various checks on the calibrations, such as comparison with previous missions, repeatability, the effects of scan speed, and observation mode. The results of the aperture photometry after applying the calibration factors derived above are listed in Tab. 7.

6.2.1. Comparison with Previous Missions

In order to check the validity of the flux calibration, we observed the 11 galaxies listed in Tab. 2, and compared their AKARI fluxes with those from IRAS and ISO.

All 11 galaxies were detected by IRAS at both 60 and 100 μm (IRAS Faint Source Catalog; Moshir et al. 1992). The predictions for the 65 and 90 μm fluxes based on the IRAS measurements were calculated as follows. First, we apply color corrections to the IRAS measurements (Beichman et al. 1988) by assuming a power-law spectrum. Then we interpolate the IRAS 60 and 100 μm measurements to the center wavelength of the AKARI bands, 65 and 90 μm . Finally, we apply color corrections to the AKARI measurements by assuming the same power law spectrum as that determined by the IRAS measurements. Figure 7 shows the IRAS-to-AKARI flux ratios as a function of the AKARI flux. The average ratios of IRAS-to-AKARI measurements are 1.04 ± 0.03 and 1.03 ± 0.03 for the *N60* and *WIDE-S* bands, respectively. This result implies that the absolute calibration of both instruments consistent to each other within the uncertainties.

Among our 11 samples, 5 famous galaxies (Arp 220, Mrk 231, IRAS 20100–4156, IRAS 15250+3609, IRAS 03158+4227) were observed by the ISO/ISOPHOT at 10 bands between 10 and 200 μm (Klaas et al. 2001). The wide wavelength coverage of ISO at longer than 100 μm enables us to compare them not only in the SW bands, but also in the LW bands. We calculate the average ratios of ISO/ISOPHOT-to-AKARI by using the same method as that of IRAS-

to-AKARI, but by assuming a gray-body spectrum given by the ISO/ISOPHOT measurement (Klaas et al. 2001) rather than a power-law spectrum. The results of the comparison are also shown in Fig. 7. The ratios of ISO-to-AKARI are 1.07 ± 0.03 , 0.98 ± 0.03 , 0.97 ± 0.13 , and 0.89 ± 0.17 for the *N60*, *WIDE-S*, *WIDE-L*, and *N160* bands, respectively. Although the number of sample is not statistically sufficient, the obtained values are equal to unity within the uncertainties.

6.2.2. Repeatability

The photometric repeatability was checked by the data of stars and galaxies that were observed twice; asteroids are not suitable for repeatability checks because of the time-variations in their fluxes. In the case of the SW bands, 6 case studies (HR 5321, HR 5430, HR 872, HR 1208, IRAS 08201+2801, and IRAS 08474+1813) are available. Except for HR 1208, two measurements in each case agree to within 10% and 3% for the *N60* and *WIDE-S* bands, respectively. As for the *WIDE-L* and *N160* bands, since there is no comparable data, we could not check the photometric repeatability.

6.2.3. Scan Speed

In order to examine the dependence of the calibration factor on the scan speed, three calibrators (Vesta, Europa, and Neptune) were observed at scan speeds of both $8'' \text{ s}^{-1}$ and $15'' \text{ s}^{-1}$. These data are listed in Tab. 7. The observed fluxes for the $15'' \text{ s}^{-1}$ data are $\sim 10\%$ fainter than those for the $8'' \text{ s}^{-1}$ data in all bands. This result implies contribution of the slow transient response of the Ge:Ga detector. However, the number of sample is statistically insufficient to give a quantitative conclusion.

6.2.4. Observation Mode

The calibration factors derived here are determined from observations by using AOT FIS01 (two round-trip scans) with a $70''$ shift length, but should also apply directly to data taken with a $240''$ shift length or with AOT FIS02 (single round-trip scan), because all of the modes conduct the same detector operation.

In order to evaluate the influence by the difference of the observation mode, we checked data for the far-infrared deep survey observed by the AKARI mission program teams FBSEP (Shirahata et al. 2009, in prep.). They observed $\sim 2 \text{ deg}^2$ area with both FIS01 and FIS02 at scan speeds of $15'' \text{ s}^{-1}$, and detected 8, 126, 4, and 1 galaxies in the *N60*, *WIDE-S*, *WIDE-L*, and *N160* bands, respectively. The obtained fluxes are consisted with each other within 3%, 1%, 6%, and 10% for the *N60*, *WIDE-S*, *WIDE-L*, and *N160* bands, respectively, which are within the uncertainties. Therefore, we concluded that there are no significant differences originated in the observation mode.

6.3. Application to the Data Reduction

We note that our photometry is performed to a point-source with a fixed sky annulus; $2'.3\text{--}3'.3$ in radius for the SW bands and $3'.0\text{--}4'.0$ in radius for the LW bands. Therefore, the

calibration factors presented here should only be applied to measurements carried out with the same parameters. Photometry using a different aperture size is possible via the application of an aperture correction factor (Tab. 5), if the target is a point-source. If the target is an extended source, proper treatment for the slow response is necessary.

Table 8 summarizes the calibration factors for point-source photometry in the FIS Slow-Scan observations. In order to measure the point-source fluxes, the signals integrated within the aperture must be divided by the calibration factor to correct the slow transient response. For the point-sources brighter than 0.4, 0.1, 2.0, and 1.5 Jy in the *N60*, *WIDE-S*, *WIDE-L*, and *N160* bands, respectively, uncertainties of the flux calibrations are larger than the measurement errors.

The FIS photometric flux is defined for a $\nu F_\nu = \text{const.}$ spectrum at the center wavelength of each band. This definition was first adopted by IRAS and used by several infrared astronomical satellites such as COBE and ISO. Also, the Spitzer/IRAC and IRS instruments use the same convention, while the Spitzer/MIPS uses a 10000 K black-body as its reference spectrum. The flux obtained using these derived calibration factors is not the actual flux, but a 'quoted' flux. Therefore, in order to obtain the monochromatic flux at the band center wavelength, we should apply a color correction depending on the SED of the target source. A color correction factor, K , is defined as $K = \Delta\nu_{\text{SED}}/\Delta\nu_{\text{flat}} = F_{\text{obtained}}/F_{\text{real}}$, where $\Delta\nu$ is the effective band width. Color correction factors assuming a gray-body spectrum and a power-law spectrum are shown in Tab. 9.

7. Summary

We performed flux calibrations for the FIS Slow-Scan observations, based on the measurements of stars and asteroids. We described in detail the data reduction and aperture photometric procedures that we used for the calibration sources. The expected fluxes of the calibration sources are lying in a wide flux range from 0.1 Jy to 400 Jy. There was a systematic flux dependence between the observed flux and the expected flux of the calibration sources, which was attributed to the slow transient response of the Ge:Ga detector. The calibration accuracies for the point-sources were estimated to be 14%, 13%, 10%, and 50% for the *N60*, *WIDE-S*, *WIDE-L*, and *N160* bands, respectively. The calibration scheme described in this paper will be useful for future missions, such as Herschel and SPICA.

AKARI is a JAXA project with the participation of ESA. We thank all of the members of the AKARI project for their continuous help and support. We would also express our gratitude to the FIS hardware and software team for their devoted work in developing the FIS instruments and its data reduction tool kit. The FIS was developed in collaboration with the ISAS/JAXA, Nagoya University, the University of Tokyo, the National Institute of Information and Communications Technology (NICT), the National Astronomical Observatory

of Japan (NAOJ), and other research institutes. We are grateful to S. Oyabu for help with the development of the reduction tools. We thank to M. Fukagawa and T. Hirao for valuable discussions. We thank to W.-S. Jeong for providing the data of the optical simulation model of PSF, and thank to R. Moreno for providing flux model of Neptune. This work is partly supported by JSPS grants (16204013 and 19540250). M. Cohen thanks ISAS/JAXA for supporting a visit to Tokyo to participate in this work. S. Hasegawa was supported by Space Plasma Laboratory, ISAS/JAXA.

References

- Abraham, P., Leinert, C., & Lemke, D. 1997, *A&A*, 328, 702
- Beichman, C. A., Neugebauer, G., Habing, H. J., Clegg, P. E., Chester, T. J. 1988, *Infrared astronomical satellite (IRAS) catalog and atlases. Volume 1: Explanatory supplement* (Washington, DC:GPO)
- Blommaert, J. A. D. L., et al. 2003, *The ISO Handbook, Vol. 2, CAM—The ISO Camera* (ESA SP-1262; Noordwijk: ESA)
- Cohen, M., Walker, R. G., Carter, B., Hammersley, P., Kidger, M., & Noguchi, K. 1999, *AJ*, 117, 1864
- Cohen, M., Megeath, S. T., Hammersley, P. L., Martin-Luis, F., & Stauffer, J. 2003, *AJ*, 125, 2645
- Cohen, M., Wheaton, W. A., & Megeath, S. T. 2003, *AJ*, 126, 1090
- Doi, Y., et al. 2002, *Adv. Space Res.*, 30, 2099
- Fouks, B. I., & Schubert, J. 1995, in *Infrared Detectors and Instrumentation for Astronomy*, ed. A. M. Fowler (Proc. of SPIE), 2475, 487
- Fujiwara, M., Hirao, T., Kawada, M., Shibai, H., Matsuura, S., Kaneda, H., Patrashin, M. A., & Nakagawa, T. 2003, *Appl. Opt.*, 42, 2166
- Gordon, K. D., et al. 2007, *PASP*, 119, 1019
- Haegel, N. M., Simoes, J. C., White, A. M., & Beeman, J. W. 1999, *Appl. Opt.*, 38, 1910
- Hauser, M. G., Kelsall, T., Leisawitz, D., & Weiland, J. 1998, *COBE Diffuse Infrared Background Experiment (DIRBE) Explanatory Supplement* (Greenbelt: NASA)
- Hiromoto, N. & Fujiwara, M. 1999, *Infrared Physics & Technology*, 40, 387
- Jeong, W.-S., et al. 2003, *PASJ*, 55, 717
- Kaneda, H., Okamura, Y., Nakagawa, T., & Shibai, H. 2002, *Adv. Space Res.*, 30, 2105
- Kaneda, H., Kim, W., Onaka, T., Wada, T., Ita, Y., Sakon, I., & Takagi, T. 2007, *PASJ*, 59, S423
- Kawada, M., et al. 2007, *PASJ*, 59, S389
- Kawada, M. et al. 2008, *PASJ*, 60, S389
- Klaas, U., et al. 2001, *A&A*, 379, 823
- Landsman, W. B. 1993, in *ASP Conf. Ser.*, 52, *Astronomical Data Analysis Software and Systems II*, ed. R. J. Hanish, R. J. V. Brissenden, & J. Barnes (SanFrancisco: ASP), 246
- Matsuura, S., et al. 2007, *PASJ*, 59, S503
- Matsuura, S., et al. 2009, in prep.
- Moreno, R. 1998, Ph.D. Thesis. Université Paris VI

- Moshir, M., Kopman, G., & Conrow, T. A. O. 1992, *IRAS Faint Source Survey, Explanatory Supplement*, version 2 (Pasadena: IPAC)
- Müller, T. G. & Lagerros, J. S. V. 1998, *A&A*, 338, 340
- Müller, T. G. & Lagerros, J. S. V. 2002, *A&A*, 381, 324
- Müller, T. G. & Lagerros, J. S. V. 2003, *The calibration legacy of the ISO Mission*, ed. L. Metcalfe, A. Salama, S. B. Peschke & M. F. Kessler (ESA SP-481), 157
- Murakami, H., et al. 2007, *PASJ*, 59, S369
- Murakami, N., et al. 2008, in prep.
- Nagata, H., Shibai, H., Hirao, T., Watabe, T., Noda, M., Hibi, Y., Kawada, M., & Nakagawa, T. 2004, *IEEE Trans. Electron Devices*, 51, 270
- Nakagawa, T., et al. 2007, *PASJ*, 59, S377
- Schulz, B., et al. 2002, *A&A*, 381, 1110
- Shirahata, M., et al. 2003, in *Optical, Infrared, and Millimeter Space Telescopes*, ed. J. C. Mather (Proc. of SPIE), 4859, 162
- Shirahata, M., et al. 2009, in prep.
- Stansberry, J. A., et al. 2007, *PASP*, 119, 1038
- Suzuki, T., et al. 2008, *PASP*, 120, 895
- Verdugo, E., Yamamura, I., Pearson, C., Shirahata, M., Matsuura, S., Okada, Y., Makiuti, S., Murakami, N., & Kawada, M. 2007, *AKARI FIS Data Users Manual Version 1.3*
- Williams, R. E., et al. 1996, *AJ*, 112, 1335

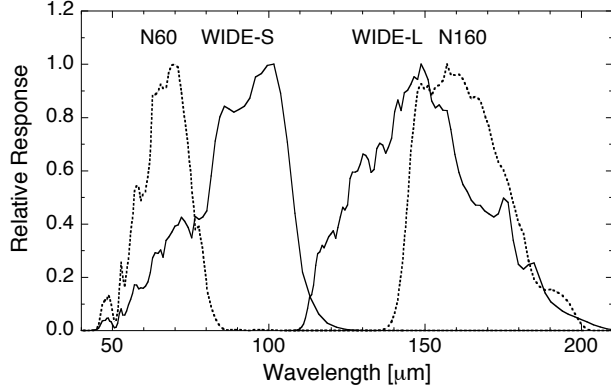


Fig. 1. The system spectral response of the FIS photometric bands. These profiles were derived from the spectral response of optical components and the detector spectral responsivity. These profiles provide typical band shape, because detectors have the pixel-to-pixel variation of the spectral responsivity.

Table 1. Specification for the FIS instrument in photometry mode.

Band name	<i>N60</i>	<i>WIDE-S</i>	<i>WIDE-L</i>	<i>N160</i>	
Center wavelength	65	90	140	160	[μm]
Wavelength range	50–80	60–110	110–180	140–180	[μm]
Array format	20 \times 2	20 \times 3	15 \times 3	15 \times 2	[pixels]
Pixel scale*	26.8 \times 26.8		44.2 \times 44.2		[arcsec ²]
Pixel pitch*	29.5 \times 29.5		49.1 \times 49.1		[arcsec ²]
Detector device	Monolithic Ge:Ga Array		Stressed Ge:Ga Array		

Notes.

* at the center of the field of view.

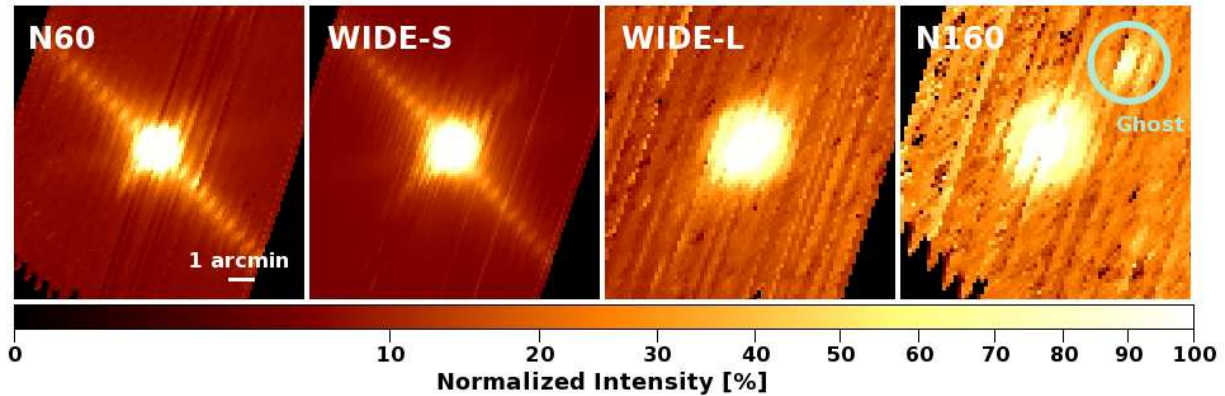


Fig. 2. Examples of the final co-added image obtained by the FIS Slow-Scan observation mode (AOT FIS01). The panels show *N60*, *WIDE-S*, *WIDE-L*, and *N160* images from left to right. The image size is $10' \times 10'$. The color scale is square root contours. In the images of the *N60* and *WIDE-S* bands, cross-talk signals are seen along both array axes. Ghost signals are seen in all bands, especially in the *N160* band.

Table 2. Observation log and expected flux.

Target name	Observation		Expected flux [†]				Accuracy [%]
	Date	AOT parameter*	<i>N60</i> [Jy]	<i>WIDE-S</i> [Jy]	<i>WIDE-L</i> [Jy]	<i>N160</i> [Jy]	
HR 5826	2006/04/21 20:38:35	2.0;8;70	0.338	0.237	0.064	0.052	6
HR 5321	2006/04/22 06:31:28	2.0;8;70	0.276	0.193	0.053	0.043	6
HR 5321 (2)	2006/04/22 11:28:30	2.0;8;70	0.276	0.193	0.053	0.043	6
HR 5430	2006/04/28 04:27:17	2.0;8;70	0.543	0.380	0.104	0.084	6
HR 5430 (2)	2006/04/28 06:06:18	2.0;8;70	0.543	0.380	0.104	0.084	6
HR 1208	2006/04/29 15:57:40	1.0;8;70	2.864	2.006	0.545	0.441	6
HR 872	2006/04/30 00:11:43	2.0;8;70	0.214	0.150	0.041	0.033	6
HR 872 (2)	2006/04/30 01:50:45	2.0;8;70	0.214	0.150	0.041	0.033	6
HR 1208 (2)	2006/05/02 01:43:26	1.0;8;70	2.864	2.006	0.545	0.441	6
Alpha CMa	2006/10/07 18:28:06	2.0;8;70	3.290	2.293	0.616	0.497	1.47
Alpha Boo	2007/01/15 00:02:26	1.0;8;70	18.689	13.089	3.558	2.879	6
Alpha Tau	2007/02/28 14:18:57	1.0;8;70	17.042	11.939	3.249	2.630	6
HD 216386	2007/06/03 01:05:46	2.0;8;70	2.177	1.524	0.414	0.335	6
HD 98118	2007/06/10 01:17:14	2.0;8;70	0.330	0.232	0.063	0.051	6
HD 222643	2007/06/11 01:23:08	2.0;8;70	0.142	0.099	0.027	0.022	6
HD 224935	2007/06/20 00:48:29	2.0;8;70	1.869	1.309	0.355	0.288	6
HD 053501	2007/07/13 02:52:02	2.0;8;70	0.175	0.122	0.033	0.027	6
HD 92305	2007/08/23 12:12:43	2.0;8;70	0.906	0.636	0.173	0.140	6
241 Germania	2006/04/27 15:44:31	0.5;8;70	8.958	6.932	2.356	1.940	12.5
241 Germania (2)	2006/04/27 23:59:37	0.5;8;70	7.813	6.064	2.073	1.707	12.5
6 Hebe	2006/04/30 03:07:09	0.5;8;70	25.258	19.382	6.469	5.313	5
6 Hebe (2)	2006/05/01 00:34:26	0.5;8;70	25.681	19.699	6.570	5.396	5
511 Davida	2006/05/02 22:50:20	0.5;8;70	18.394	14.387	4.999	4.127	7.5
511 Davida (2)	2006/05/03 12:02:32	0.5;8;70	18.185	14.214	4.933	4.071	7.5
7 Iris	2006/08/01 18:19:43	0.5;8;70	56.355	42.927	14.103	11.554	20
2 Pallas	2006/09/27 06:20:31	0.5;8;70	59.254	46.375	16.142	13.329	10
1 Ceres	2006/11/08 14:58:11	0.5;8;70	264.848	206.126	70.786	58.327	5
93 Minerva	2006/11/20 00:42:13	1.0;8;70	7.551	5.873	2.017	1.662	7.5
65 Cybele	2006/12/28 00:16:17	1.0;8;70	15.192	11.905	4.155	3.431	5
4 Vesta	2007/02/23 22:33:11	0.5;8;70	200.598	147.871	44.748	36.486	7.5
4 Vesta (2)	2007/02/24 00:12:31	0.5;15;70	202.519	149.228	45.113	36.778	7.5
52 Europa	2007/04/14 23:08:31	0.5;8;70	24.150	18.807	6.467	5.328	5
52 Europa (2)	2007/04/15 22:19:51	0.5;15;70	24.328	18.941	6.511	5.364	5
Neptune	2007/05/13 01:22:57	0.5;8;70	315.942	361.867	265.605	248.897	5
Neptune (2)	2007/05/13 19:36:26	0.5;15;70	316.215	362.171	265.833	249.113	5
47 Aglaja	2007/06/26 01:48:04	2.0;8;70	7.008	5.423	1.844	1.518	7.5
511 Davida (3)	2007/07/20 03:36:26	0.5;8;70	20.743	16.175	5.576	4.592	7.5
IRAS 08201+2801	2006/04/22 01:17:21	0.5;8;70	–	–	–	–	–
IRAS 08201+2801 (2)	2006/04/22 02:56:21	0.5;8;70	–	–	–	–	–
IRAS 08591+5248	2006/04/22 04:42:28	0.5;8;70	–	–	–	–	–
IRAS 08572+3915	2006/04/26 01:03:51	0.5;8;70	–	○	–	–	–
IRAS 08474+1813	2006/04/30 03:59:18	0.5;8;70	–	–	–	–	–
IRAS 08474+1813 (2)	2006/04/30 05:38:20	0.5;8;70	–	–	–	–	–
Arp 220	2006/08/06 06:45:02	0.5;8;70	○	○	○	○	–
Mrk 231	2006/12/01 19:20:05	0.5;8;70	○	○	–	–	–
IRAS 20100–4156	2007/04/16 23:17:36	1.0;8;70	–	○	–	–	–
UGC 05101	2007/04/22 12:44:18	0.5;8;70	○	○	–	–	–
IRAS 00188–0856	2007/06/23 01:45:19	2.0;8;70	–	○	–	–	–
IRAS 15250+3609	2007/07/28 03:16:26	2.0;8;70	–	○	–	–	–
IRAS 03158+4227	2007/08/23 11:35:18	2.0;8;70	–	○	–	–	–

Notes.

* FIS01 AOT parameter : Reset interval [s]; scan speed [arcsec sec⁻¹]; shift length [arcsec].

† Model calculation : Stars; Cohen et al. 1999, 2003a, 2003b, Asteroids; Müller & Lagerros 1998, 2002, Neptune; Moreno 1998.

The data designated with the bold-faced or ○ symbol is data used for the measurements of PSFs and the encircled energy function.

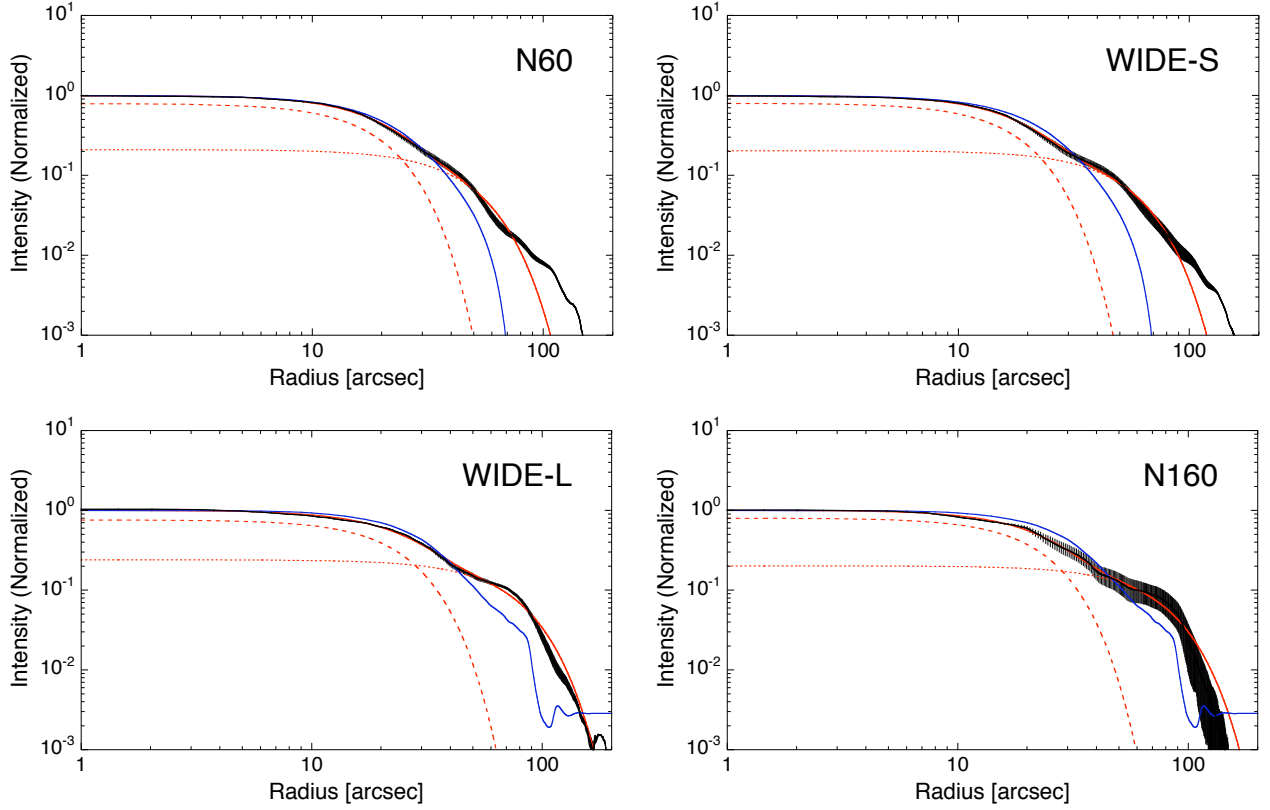


Fig. 3. Radial profiles of the observed PSFs and the optical simulation model. The observed profiles (black solid lines) are derived from the observation of bright point-sources. The error bars indicate the standard deviation. The results of the two component Gaussian fitting are represented by red solid lines (total) and red dotted lines (each component). The expected profiles from the optical simulation model are shown by blue solid lines.

Table 3. Gaussian fitting parameters for the PSFs.

Band name	<i>N60</i>	<i>WIDE-S</i>	<i>WIDE-L</i>	<i>N160</i>	
Main component:					
- Intensity (A)	79.03 ± 0.33	79.68 ± 0.23	76.01 ± 0.38	79.86 ± 0.30	[%]
- FWHM (based on σ_1)	32.05 ± 0.10	30.17 ± 0.08	40.85 ± 0.10	38.23 ± 0.15	[arcsec]
Sub component:					
- Intensity (1-A)	20.97 ± 0.35	20.33 ± 0.24	23.99 ± 0.39	20.14 ± 0.30	[%]
- FWHM (based on σ_2)	77.51 ± 0.57	86.01 ± 0.53	118.98 ± 1.03	120.62 ± 0.51	[arcsec]

Notes.

Two components Gaussian function: $I(x) = A \exp(-(x^2)/2\sigma_1^2) + (1 - A) \exp(-(x^2)/2\sigma_2^2)$;

A = Intensity of main component; $\sigma = \text{FWHM}/2\sqrt{2\ln 2}$.

Table 4. Information of the ghost signal.

Detector	SW (<i>N60</i> ↔ <i>WIDE-S</i>)	LW (<i>WIDE-L</i> ↔ <i>N160</i>)	
Relative position*			
- In-scan	5.4	3.6	[arcmin]
- Cross-scan	0.2	2.0	[arcmin]
- Distance	5.4	4.1	[arcmin]
Intensity [†]	~1	~10	[%]

Note.

The ghost signal appears in one array when a strong light enters the other array of the same detector.

* The relative position of the ghost image from the target source.

† The intensity of the ghost signal compared with the target signal observed in the other array.

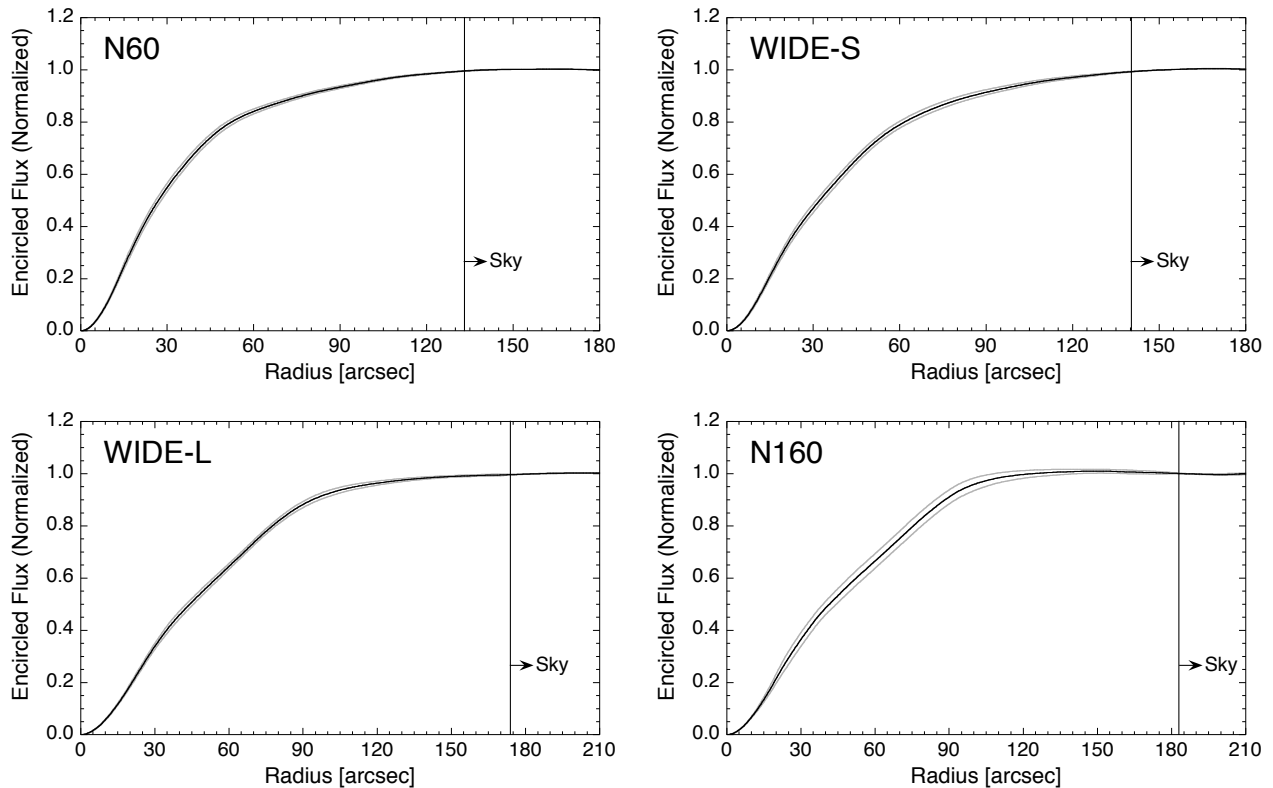


Fig. 4. Encircled energy function. The gray region indicates the range of the standard deviation of sample. All profiles are normalized to 1.0 at the sky region.

Table 5. Aperture correction factors.

Aperture*	<i>N60</i>	<i>WIDE-S</i>	<i>WIDE-L</i>	<i>N160</i>
5	0.030 ± 0.002	0.028 ± 0.002	0.015 ± 0.001	0.018 ± 0.001
10	0.112 ± 0.005	0.105 ± 0.006	0.056 ± 0.002	0.066 ± 0.003
15	0.225 ± 0.010	0.208 ± 0.010	0.116 ± 0.004	0.133 ± 0.009
20	0.340 ± 0.014	0.310 ± 0.014	0.187 ± 0.007	0.214 ± 0.018
25	0.440 ± 0.016	0.397 ± 0.016	0.264 ± 0.009	0.293 ± 0.025
30	0.524 ± 0.016	0.469 ± 0.017	0.337 ± 0.011	0.363 ± 0.026
35	0.596 ± 0.016	0.534 ± 0.016	0.402 ± 0.014	0.428 ± 0.026
40	0.659 ± 0.015	0.596 ± 0.016	0.458 ± 0.015	0.484 ± 0.026
45	0.715 ± 0.014	0.655 ± 0.015	0.507 ± 0.014	0.532 ± 0.027
50	0.762 ± 0.013	0.708 ± 0.014	0.554 ± 0.013	0.578 ± 0.028
55	0.799 ± 0.011	0.753 ± 0.014	0.599 ± 0.012	0.622 ± 0.028
60	0.826 ± 0.010	0.789 ± 0.013	0.644 ± 0.011	0.664 ± 0.028
65	0.847 ± 0.009	0.818 ± 0.013	0.689 ± 0.010	0.708 ± 0.028
70	0.865 ± 0.008	0.844 ± 0.013	0.734 ± 0.010	0.751 ± 0.028
75	0.882 ± 0.007	0.865 ± 0.012	0.778 ± 0.010	0.795 ± 0.028
80	0.897 ± 0.007	0.884 ± 0.012	0.817 ± 0.011	0.837 ± 0.028
85	0.911 ± 0.006	0.900 ± 0.011	0.852 ± 0.012	0.875 ± 0.028
90	0.923 ± 0.006	0.913 ± 0.010	0.881 ± 0.012	0.910 ± 0.027
95	0.934 ± 0.005	0.926 ± 0.009	0.904 ± 0.012	0.938 ± 0.026
100	0.944 ± 0.005	0.937 ± 0.008	0.922 ± 0.012	0.958 ± 0.024
105	0.954 ± 0.004	0.947 ± 0.007	0.936 ± 0.011	0.973 ± 0.022
110	0.963 ± 0.004	0.957 ± 0.006	0.948 ± 0.010	0.983 ± 0.019
115	0.971 ± 0.003	0.964 ± 0.005	0.956 ± 0.009	0.991 ± 0.017
120	0.977 ± 0.003	0.971 ± 0.005	0.963 ± 0.008	0.996 ± 0.015
125	0.982 ± 0.002	0.976 ± 0.004	0.969 ± 0.007	1.001 ± 0.013
130	0.987 ± 0.002	0.983 ± 0.003	0.975 ± 0.006	1.004 ± 0.012
135	0.991 ± 0.002	0.988 ± 0.002	0.979 ± 0.005	1.006 ± 0.010
140			0.983 ± 0.004	1.007 ± 0.009
145			0.986 ± 0.004	1.009 ± 0.008
150			0.989 ± 0.003	1.009 ± 0.007
155			0.991 ± 0.003	1.009 ± 0.007
160			0.992 ± 0.004	1.007 ± 0.007
165			0.994 ± 0.004	1.006 ± 0.007
170			0.995 ± 0.003	1.004 ± 0.006
175			0.996 ± 0.002	1.003 ± 0.005
180			0.998 ± 0.001	1.001 ± 0.003

Notes.

* Aperture radius [arcsec]

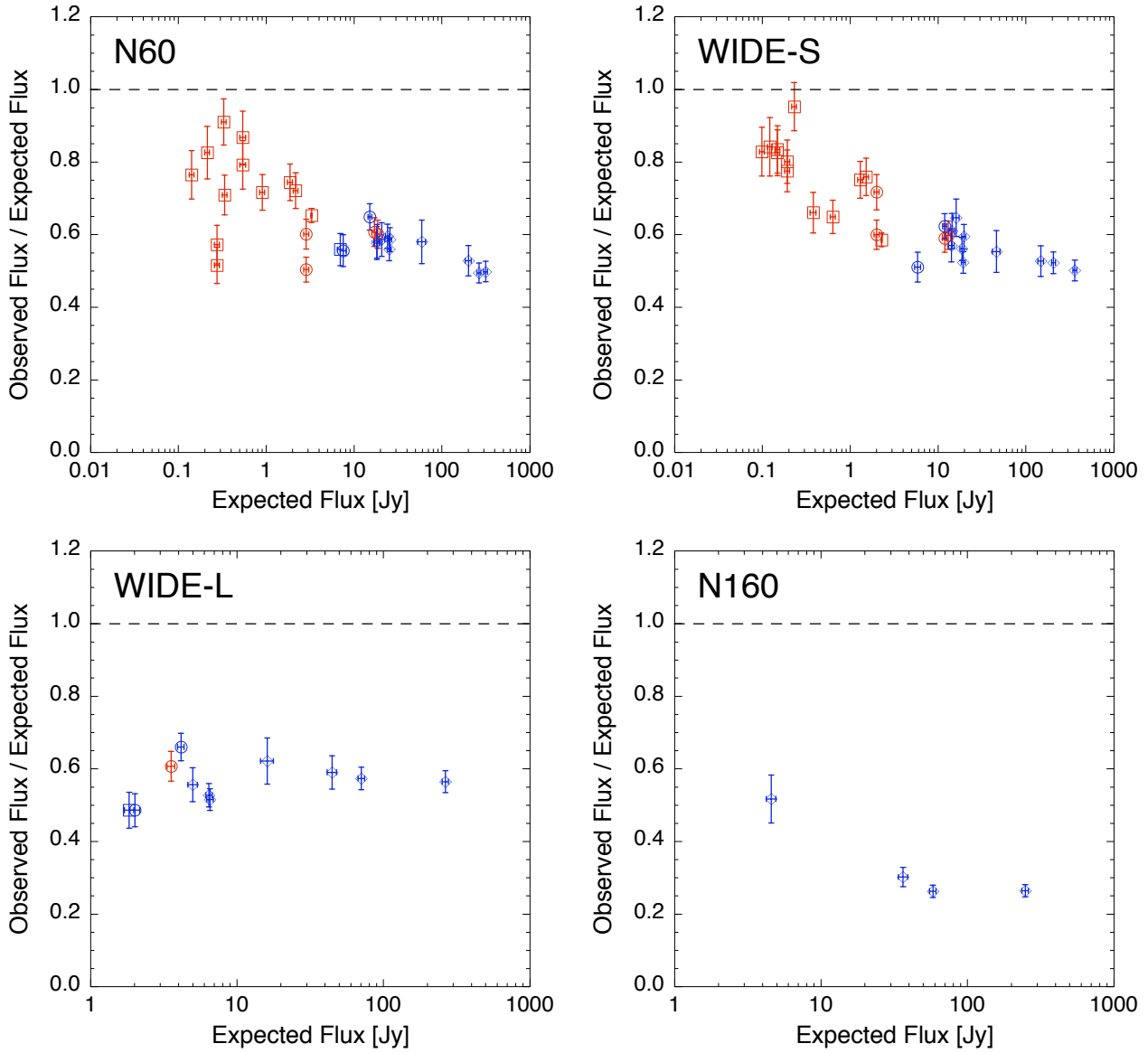


Fig. 5. The observed-to-expected flux ratio as a function of the expected flux. The error bars on the y-axis represent the combined uncertainty of measurement errors and model uncertainties. The red and blue symbols denote stars and asteroids, respectively. The squares, circles, and diamonds are the data with reset intervals of 2, 1, and 0.5 sec, respectively. The dashed lines indicate a linear relation.

Table 6. Beam solid angles.

Band name	Beam solid angle* [sr]
<i>N60</i>	$(4.06 \pm 0.10) \times 10^{-8}$
<i>WIDE-S</i>	$(4.81 \pm 0.13) \times 10^{-8}$
<i>WIDE-L</i>	$(9.92 \pm 0.19) \times 10^{-8}$
<i>N160</i>	$(10.21 \pm 0.42) \times 10^{-8}$

Note.

* The beam solid angles: $\pi r^2 \times$ (Aperture correction factors at r);

$r = 40''$ (for the *N60* and *WIDE-S* bands);

$r = 60''$ (for the *WIDE-L* and *N160* bands).

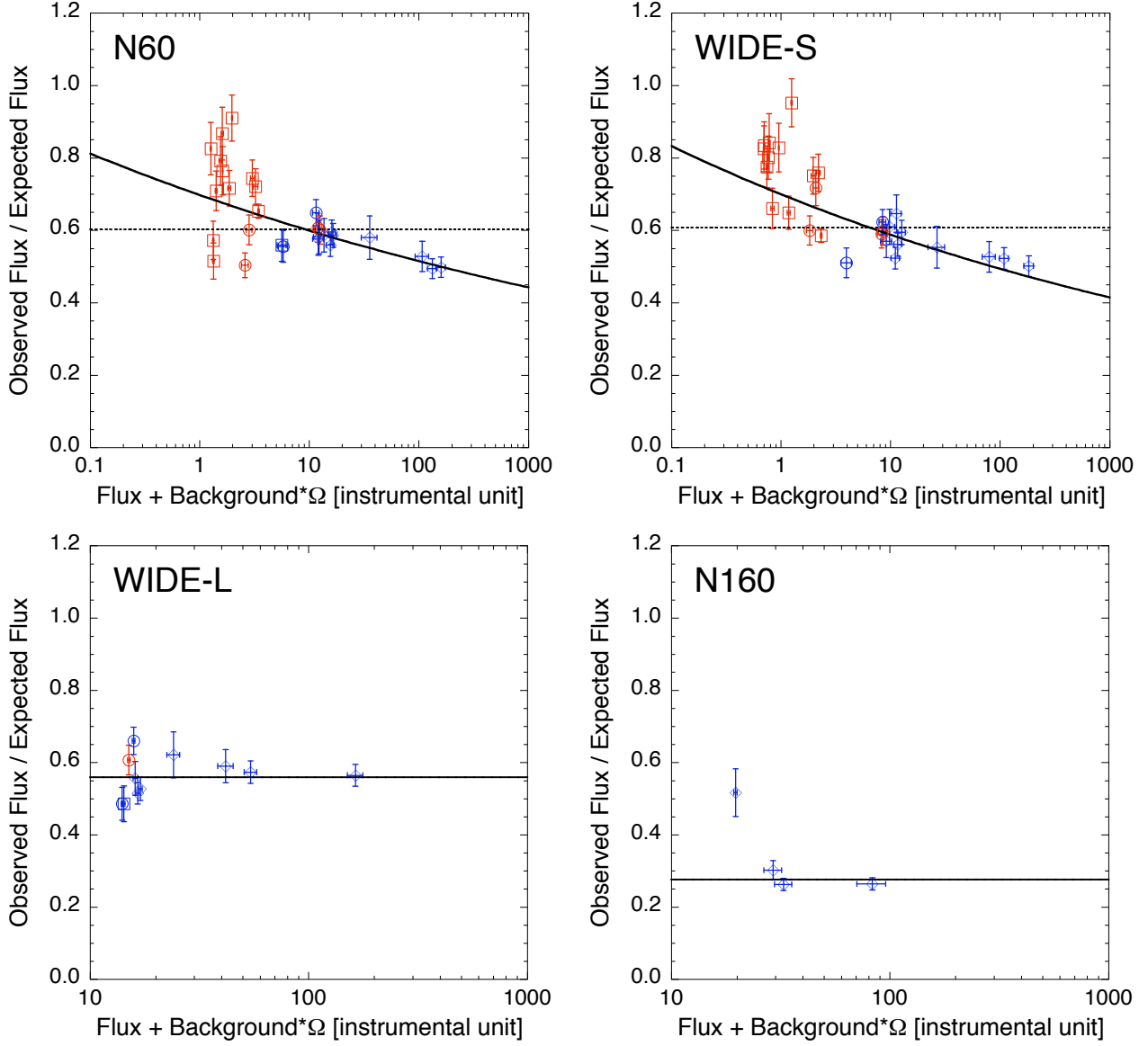


Fig. 6. The observed-to-expected flux ratio as a function of the total observed flux including the background flux and the dark current. The color and symbols are the same as those in Fig. 5. The solid lines for the SW bands are the results of the power-law fit; $y = 0.698 \times x^{-0.0659}$ (*N60*), $y = 0.700 \times x^{-0.0757}$ (*WIDE-S*). The dashed lines for the SW bands and the solid lines for the LW bands are the weighted average; $y = 0.560$ (*WIDE-L*), $y = 0.277$ (*N160*).

Table 7. Results of observation.

Target name	Observed flux [Jy]			
	<i>N60</i>	<i>WIDE-S</i>	<i>WIDE-L</i>	<i>N160</i>
HR 5826	0.351 ± 0.013	–	–	–
HR 5321	0.208 ± 0.011	0.209 ± 0.007	–	–
HR 5321 (2)	0.230 ± 0.012	0.216 ± 0.008	–	–
HR 5430	0.696 ± 0.022	–	–	–
HR 5430 (2)	0.634 ± 0.020	0.354 ± 0.012	–	–
HR 1208	2.199 ± 0.064	1.798 ± 0.048	–	–
HR 872	0.257 ± 0.012	0.172 ± 0.007	–	–
HR 872 (2)	–	0.174 ± 0.007	–	–
HR 1208 (2)	2.641 ± 0.077	2.172 ± 0.058	–	–
Alpha CMa	3.337 ± 0.097	2.045 ± 0.056	–	–
Alpha Boo	19.009 ± 0.655	13.163 ± 0.403	3.855 ± 0.101	–
Alpha Tau	17.452 ± 0.598	11.815 ± 0.360	–	–
HD 216386	2.430 ± 0.070	1.753 ± 0.047	–	–
HD 98118	0.450 ± 0.014	0.321 ± 0.009	–	–
HD 222643	0.161 ± 0.007	0.117 ± 0.005	–	–
HD 224935	2.143 ± 0.062	1.478 ± 0.039	–	–
HD 053501	–	0.144 ± 0.008	–	–
HD 92305	0.968 ± 0.028	0.596 ± 0.018	–	–
241 Germania	10.249 ± 0.329	7.795 ± 0.226	2.806 ± 0.109	–
241 Germania (2)	10.390 ± 0.334	7.855 ± 0.228	2.578 ± 0.107	–
6 Hebe	24.248 ± 0.865	17.382 ± 0.553	–	–
6 Hebe (2)	25.937 ± 0.934	20.272 ± 0.658	6.046 ± 0.156	–
511 Davida	18.076 ± 0.621	14.896 ± 0.465	4.966 ± 0.144	–
511 Davida (2)	17.690 ± 0.606	13.687 ± 0.423	–	–
7 Iris	67.823 ± 2.803	57.474 ± 2.166	32.242 ± 0.727	15.984 ± 0.675
2 Pallas	62.331 ± 2.544	46.987 ± 1.719	17.907 ± 0.414	–
1 Ceres	258.977 ± 12.991	219.497 ± 10.082	72.467 ± 1.619	55.259 ± 2.286
93 Minerva	6.746 ± 0.208	4.749 ± 0.132	1.750 ± 0.065	–
65 Cybele	16.579 ± 0.564	12.446 ± 0.380	4.897 ± 0.122	–
4 Vesta	206.512 ± 10.038	155.047 ± 6.779	47.163 ± 1.064	39.749 ± 1.652
4 Vesta (2)	156.430 ± 7.310	117.833 ± 4.951	37.654 ± 0.887	–
52 Europa	24.736 ± 0.887	18.149 ± 0.582	6.093 ± 0.168	–
52 Europa (2)	22.525 ± 0.797	17.675 ± 0.565	5.879 ± 0.260	–
Neptune	314.872 ± 16.229	384.606 ± 19.106	267.687 ± 5.937	238.428 ± 9.814
Neptune (2)	315.032 ± 16.237	366.421 ± 18.082	233.951 ± 5.221	199.637 ± 8.253
47 Aglaja	6.289 ± 0.193	–	1.600 ± 0.069	–
511 Davida (3)	20.701 ± 0.723	17.935 ± 0.572	–	8.568 ± 0.420
IRAS 08201+2801	1.054 ± 0.035	1.147 ± 0.032	–	–
IRAS 08201+2801 (2)	1.074 ± 0.033	1.128 ± 0.031	–	–
IRAS 08591+5248	0.630 ± 0.026	1.058 ± 0.030	–	–
IRAS 08572+3915	6.039 ± 0.184	5.494 ± 0.154	2.085 ± 0.090	–
IRAS 08474+1813	1.241 ± 0.037	1.495 ± 0.039	0.572 ± 0.062	–
IRAS 08474+1813 (2)	1.197 ± 0.036	1.461 ± 0.039	1.124 ± 0.073	–
Arp 220	117.838 ± 5.280	137.905 ± 5.920	86.655 ± 1.935	73.970 ± 3.060
Mrk 231	30.019 ± 1.101	28.917 ± 0.983	20.411 ± 0.461	17.709 ± 0.738
IRAS 20100–4156	4.664 ± 0.139	4.896 ± 0.136	–	–
UGC 05101	10.570 ± 0.340	15.788 ± 0.494	15.529 ± 0.358	13.973 ± 0.584
IRAS 00188–0856	2.616 ± 0.076	2.599 ± 0.070	2.027 ± 0.089	–
IRAS 15250+3609	5.958 ± 0.180	4.927 ± 0.136	–	–
IRAS 03158+4227	3.701 ± 0.109	3.961 ± 0.109	–	–

Notes.

The data designated with the bold-faced were used for the derivation of the calibration factors.

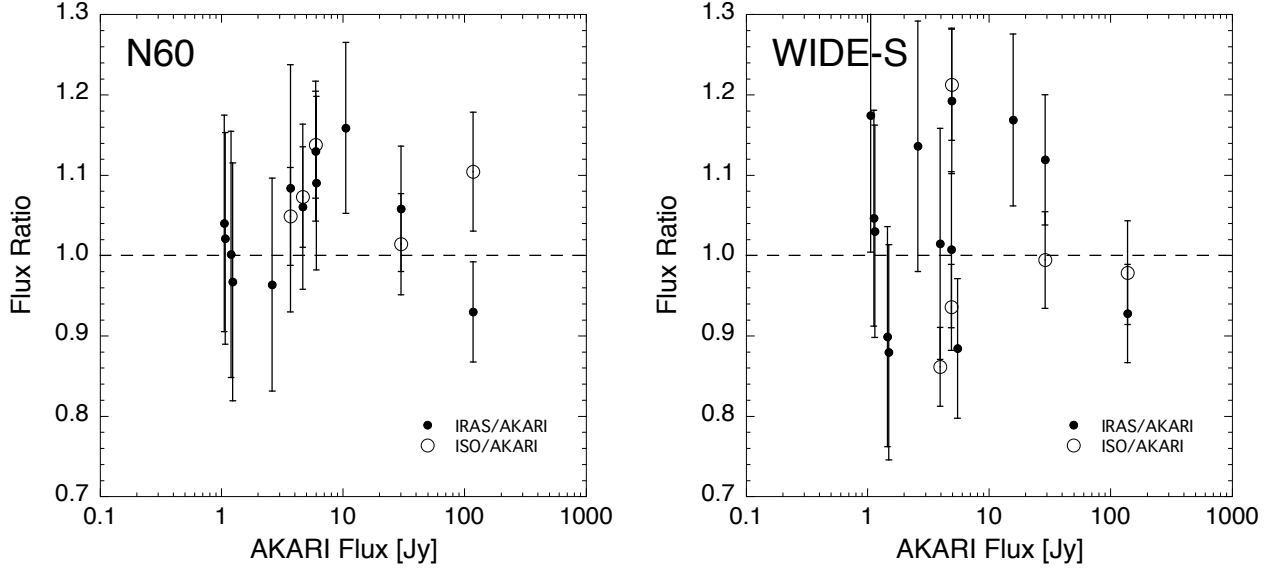


Fig. 7. The comparisons of AKARI flux with IRAS and ISO. The filled circles represent the flux ratio of AKARI-to-IRAS, while the opened circles represent the flux ratio of AKARI-to-ISO/ISPHOTO. The plots were not displayed for the *WIDE-L* and *N160* bands, because there were only two comparable data points.

Table 8. Summary of the calibration factors for point-source photometry.

Band name	Calibration factor*	Calibration accuracy [%]	Flux range [†] [Jy]
<i>N60</i>	$0.698 \times (\text{total flux})^{-0.0659}$	13.7	0.1–300
<i>WIDE-S</i>	$0.700 \times (\text{total flux})^{-0.0757}$	12.7	0.1–400
<i>WIDE-L</i>	0.560	9.97	0.5–300
<i>N160</i>	0.277	50.5	10–250

Note.

* Total flux is a sum of the observed flux, background sky flux, and the detector dark current.

† Confirmed flux range.

In the case of the fainter sources, the extrapolation should be possible, because the total fluxes are dominated by the detector dark current for the *N60* and *WIDE-S* bands, and the offset light signal for the *WIDE-L* and *N160* bands, respectively.

The brighter end is almost comparable to the saturation limit.

Table 9. Color correction factors.

Intrinsic spectrum	<i>N60</i> (65 μm)	<i>WIDE-S</i> (90 μm)	<i>WIDE-L</i> (140 μm)	<i>N160</i> (160 μm)
Black-body* ($\beta = 0$)				
- $T = 10$	4.434	1.840	1.549	1.097
- $T = 30$	1.050	0.892	0.957	0.986
- $T = 50$	0.976	0.979	0.937	0.986
- $T = 70$	0.978	1.066	0.935	0.988
- $T = 100$	0.992	1.154	0.935	0.989
- $T = 300$	1.029	1.320	0.936	0.992
- $T = 1000$	1.044	1.381	0.937	0.993
- $T = 3000$	1.048	1.398	0.937	0.993
- $T = 10000$	1.049	1.404	0.937	0.993
Gray-body* ($\beta = -1$)				
- $T = 10$	5.248	2.093	1.770	1.143
- $T = 30$	1.107	0.902	0.999	0.994
- $T = 50$	0.997	0.935	0.962	0.989
- $T = 70$	0.983	0.986	0.953	0.989
- $T = 100$	0.985	1.041	0.949	0.989
- $T = 300$	1.005	1.148	0.945	0.990
- $T = 1000$	1.013	1.187	0.944	0.990
- $T = 3000$	1.016	1.198	0.943	0.990
- $T = 10000$	1.016	1.202	0.943	0.990
Gray-body* ($\beta = -2$)				
- $T = 10$	6.281	2.396	2.048	1.198
- $T = 30$	1.178	0.930	1.060	1.008
- $T = 50$	1.030	0.918	1.003	0.998
- $T = 70$	1.001	0.944	0.987	0.995
- $T = 100$	0.992	0.976	0.978	0.994
- $T = 300$	0.995	1.041	0.968	0.993
- $T = 1000$	0.999	1.065	0.965	0.992
- $T = 3000$	1.000	1.072	0.964	0.992
- $T = 10000$	1.001	1.075	0.964	0.992
Power-law [†]				
- $\alpha = -3$	1.040	0.954	1.129	1.033
- $\alpha = -2$	1.013	0.962	1.054	1.013
- $\alpha = -1$	1.000	1.000	1.000	1.000
- $\alpha = 0$	1.001	1.076	0.964	0.992
- $\alpha = 1$	1.017	1.203	0.943	0.990
- $\alpha = 2$	1.049	1.407	0.937	0.993
- $\alpha = 3$	1.101	1.724	0.945	1.001

Note.

* Black-body and Gray-body spectrum : $F(\nu) \propto B_\nu(T) \cdot \nu^\beta$.

† Power-law spectrum : $F(\nu) \propto \nu^\alpha$.